Projection Dynamics in Godunov-Type Schemes

Kun Xu and Jishan Hu

Department of Mathematics, Hong Kong University of Science and Technology,
Clear Water Bay, Kowloon, Hong Kong
E-mail: makxu@uxmail.ust.hk, majhu@uxmail.ust.hk

There are two stages in the first-order Godunov-type schemes to update flow variables: the gas evolution stage for the numerical fluxes across a cell interface and the projection stage for the reconstruction of constant state inside each cell. Ideally, the evolution stage should be based on the exact Euler solution, the so-called Riemann solver. In this paper, we will show that some anomalous phenomena, such as postshock oscillations, density fluctuation in the 2D shear wave, and pressure wiggles at material interface in multicomponent flow calculations, are generated by dynamical effects in the projection stage. Based on a physical model, we are going to analyze qualitatively the averaging mechanism and compare our theoretical analysis with numerical observations. © 1998 Academic Press

1. INTRODUCTION

In the past two decades there has been tremendous progress in the development of numerical methods for solving the Euler equations. The most promising method is the Godunov scheme, where the Riemann solution is used for the flux evaluation, followed by the projection stage to construct a constant state inside each cell. Although the Godunov-type schemes give robust and accurate numerical solutions in most cases, they can on occasions fail quite miserably. Even the first-order Godunov method may give anomalous results, i.e. postshock oscillations, pressure wiggles in the multicomponent interface [6, 7, 14], carbuncle phenomena and odd–even decoupling [11], and pressure fluctuations in the 2D shear wave [5]. In an important paper, Quirk catalogued a number of situations in which anomalous behavior is known to occur [13]. Since then, many papers have attempted to explain these kinds of phenomena. For example, for the postshock oscillation, there exist many papers related to its observation and explanation [3, 10, 13, 14]. Arora and Roe pointed out that the intermediate states inside the shock layer do not lie on the Hugoniot curve [2]. Hence, the Riemann solver generates a whole fan of waves and induces the postshock oscillations. Jin and Liu explained this in the context of traveling wave solution and suggested that the

unsteadiness in the momentum spike is the cause of the oscillations [6]. Karni and Canic noticed that upwind scheme and Lax Friedrichs scheme behave differently here. They concluded that the vanishing viscosity in Roe's scheme at the shock region contributes to the oscillations and derived the modified parabolic equations in the shock layer [7].

The current work benefits from all previous papers. Instead of analyzing a specific flux function, we are focusing on the study of dynamical effects on the projection stage in Godunov-type schemes. In order to understand the numerical behavior of the fluid, a physical model for the dynamical averaging is constructed. It is well known that the first-order Godunov method gives dissipative numerical solutions, and it is usually interpreted as artificial viscosity effects. If the numerical fluxes are based on the exact Euler solution, the dissipation must be added somehow in the projection stage. Our focal point in this paper is to figure out qualitatively the projection mechanism, from which a few anomalous phenomena are explained, which include postshock oscillations, density fluctuation in the 2D shear wave, and pressure wiggles at material interface in multicomponent gas flow. Since the projection process is intrinsically included in all shock capturing schemes, these phenomena should be universal. We fully agree with the conclusions obtained so far that the possible cure for the postshock oscillation is to solve the viscous governing equation directly in the gas evolution stage to dissipate the oscillation generated in the projection stage. Since the projection dissipation depends on the velocity difference, in the two-dimensional case, it will be mesh-oriented. As a result, the inhomogeneity of projection dissipation and the inviscid Euler solution in gas evolution automatically trigger the shock front instabilities in the 2D case, such as the carbuncle phenomena and odd–even decoupling in the Godunov method [18].

In this paper, Section 2 analyzes the physical dynamics in the projection stage. Section 3 gives an explanation of postshock oscillations. Section 4 outlines the physical reasons for the density fluctuation in the 2D shear flow, and Section 5 explains the pressure fluctuations at material interface in multicomponent flow calculations. The last section is the conclusion.

2. PROJECTION DYNAMICS

We consider shock capturing schemes for the one dimensional Euler equations:

$$\rho_t + (\rho U)_x = 0,$$
$$(\rho U)_t + (\rho U^2 + P)_x = 0, \tag{1}$$
$$E_t + (EU + PU)_x = 0,$$

where ρ is the density, U is the velocity, ρU is the momentum, $E = \frac{1}{2}\rho U^2 + \rho e$ is the total energy, e is the internal energy, and P is the pressure. We assume that the gas is a γ-law gas, i.e. $P = (\gamma - 1)\rho e$, $1 \leq \gamma \leq 3$. In the following, we are going to construct an underlying physical model for shock-capturing schemes in solving the above equations. Based on this, some observed artifacts will be explained in the following sections.

In order to understand the dynamic effects in the projection stage, let us construct a physical model. This model is general and is not limited to the flows with shocks. Suppose there is a discontinuity in the flow distribution, and the location of the discontinuity is inside the numerical cell j. The left and right states inside cell j are (ρ_1, U_1, E_1) and (ρ_2, U_2, E_2) in regions $[x_{j-1/2}, x_{j-1/2} + \alpha \Delta x]$ and $[x_{j-1/2} + \alpha \Delta x, x_{j+1/2}]$, respectively, where Δx is the cell size (see Fig. 1). In the following, we first assume $\alpha = \frac{1}{2}$.
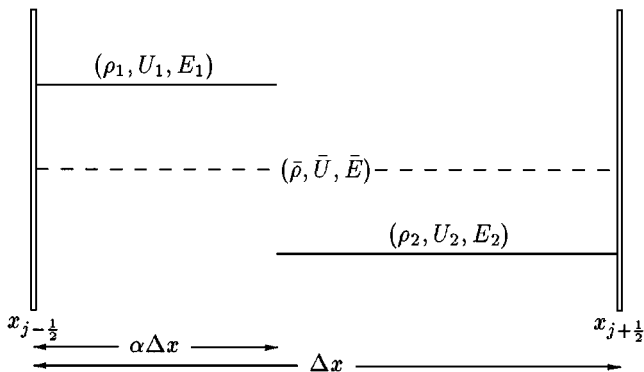
FIG. 1. Subcell mixing in the averaging stage.

The projection averaging is based on the conservation of total mass, momentum, and energy,

$$\frac{1}{2}\rho_1 + \frac{1}{2}\rho_2 = \bar{\rho}_j,$$
$$\frac{1}{2}\rho_1 U_1 + \frac{1}{2}\rho_2 U_2 = \bar{\rho}_j \bar{U}_j,$$
$$\frac{1}{2}E_1 + \frac{1}{2}E_2 = \bar{E}_j,$$

(2)

where $\bar{\rho}_j$, $\bar{\rho}_j \bar{U}_j$, $\bar{E}_j$ are the averaged mass, momentum, and energy densities in cell j. From the above equations, we have the average velocity,

$$\bar{U}_j = \frac{\rho_1 U_1 + \rho_2 U_2}{\rho_1 + \rho_2}.$$

(3)

So, after averaging, the kinetic energy in cell j becomes

$$\bar{E}_k = \frac{1}{4}(\rho_1 + \rho_2)\bar{U}_j^2.$$

(4)

However, before the averaging the original kinetic energy is

$$E_k = \frac{1}{4}\rho_1 U_1^2 + \frac{1}{4}\rho_2 U_2^2.$$

(5)

From Eq. (4) and Eq. (5), we know $E_k \geq \bar{E}_k$ and the lost kinetic energy is

$$\Delta E_k = E_k - \bar{E}_k = \frac{1}{4}\frac{\rho_1 \rho_2}{\rho_1 + \rho_2}(U_2 - U_1)^2.$$

(6)

Since the total energy is conserved in the projection stage, the decrease in kinetic energy must correspond to the increase in the thermal energy. So, the projection is actually a dissipative process to translate kinetic energy into thermal energy. From thermodynamics, we can show that the entropy is increased in the above process. The transition from initial density distributions ρ_1 and ρ_2 to the final uniform density $\frac{1}{2}(\rho_1 + \rho_2)$ is achieved through an equivalent mass diffusion process.

For the Godunov method, the flow variables inside each cell are updated through the fluxes from the gas evolution stage and the averaging in the projection stage. If the exact Euler equations are solved in the gas evolution stage, the flow behavior in the whole updating process can be approximately described by the equations (the detailed derivation is given in Appendix A)

$$\rho_t + (\rho U)_x = \epsilon \rho_{xx},$$
$$(\rho U)_t + (\rho U^2 + P)_x = \epsilon (\rho U_x)_x,$$
$$E_t + (EU + PU)_x = \frac{1}{8}\epsilon (\rho U U_x)_x,$$

(7)

where the flux terms $(\rho U, \rho U^2 + P, EU + PU)$ are obtained from the Riemann solutions in the gas evolution stage and the dissipative terms $(\epsilon \rho_{xx}, \epsilon (\rho U_x)_x, \frac{1}{8}\epsilon (\rho U U_x)_x)$ are from the projection stage. The viscous coefficient ϵ is

$$\epsilon \sim \frac{1}{2}\alpha(1-\alpha)\frac{(\Delta x)^2}{\Delta t},$$

(8)

which depends on the location of the discontinuity as shown in Fig. 1. The dependence of ϵ on Δx and Δt is due to the fact that the actual averaging process is taking place dynamically over a whole time step inside each cell, although it can be interpreted as an instantaneous process taking place at the end of each time step.

The diffusive and dissipative properties in the above model are not directly related to the specific Euler fluxes across each cell interface. Using Gilbarg and Paolucci's techniques[4], the stationary shock structure can be obtained from Eq. (7) [19], where the main conclusions are:

(1) ρ increases monotonically while U decreases, as x varies from $-\infty$ to $+\infty$;
(2) the momentum ρU is not a monotonic function of x;
(3) the maximum value of momentum ρU is independent of ϵ.

Points (1) and (2) have been analyzed based on the isentropic model in [6]. As pointed out by Jin and Liu, the momentum spike is solely related to the mass diffusion term in the continuity equation. Later, Karni and Canic found out that the the momentum spike has no direct contributions to the postshock oscillations [7]. Based on Eq. (7), we can explain the fact that the momentum peak value $(\rho U)_{max}$ is a constant. From the continuity equation, we have

$$(\rho U)_{max} \sim \epsilon (\rho_x)_{max}.$$

Since the density variation on the leading order across a shock layer is proportional to [20]

$$(\rho_x)_{max} \sim \frac{\rho_2 - \rho_1}{\delta x} \sim \frac{(\rho_2 - \rho_1)^2}{l\rho_1} \sim \frac{C_1(\rho_2 - \rho_1)^2}{\epsilon \rho_1},$$

where δx is the shock thickness, l is the mean free path, (ρ_1, ρ_2) are the upstream and downstream densities, and C_1 is the upstream sound speed. So, $(\rho U)_{max}$ can be approximated as

$$(\rho U)_{max} \sim \epsilon (\rho_x)_{max} \sim \frac{C_1(\rho_2 - \rho_1)^2}{\rho_1},$$

which is independent of ϵ. So, even with a time-dependent viscous coefficient ϵ, such as in the moving shock case, $(\rho U)_{\max}$ keeps a constant value . Theoretically, the maximum momentum peak value $(\rho U)_{\max}$ should be a universal constant for all shock capturing schemes if only projection dissipation is involved, such as the Godunov method. For the BGK scheme, the constant momentum peak value has been observed [19] for both stationary and moving shocks. All shock capturing schemes cannot converge to the Euler solutions in l^∞-norm.

3. POSTSHOCK OSCILLATIONS

The postshock oscillations have attracted much attention in the past years. The first detailed account of this problem was given by Colella and Woodward [3]. After that Roberts [14] compared different schemes and pointed out that the oscillations would occur for any schemes with flux functions that give "exact" shock resolution such as Godunov and Roe's schemes. More recently, Quirk [13], Jin and Liu [6], Arora and Roe [2], and Karni and Canic [7] have contributed greatly to the understanding and control of the oscillation. In this paper, we are concentrating on the projection dynamics to understand this phenomena.

As analyzed in [19], there is a stationary shock structure from Eq. (7) for each constant ϵ. The same conclusion has been obtained for the isentropic equations [6]. If ϵ were really a constant, such as in the stationary shock case, there would be no postshock oscillations. However, for moving shocks, the discontinuity can be located at any place inside each cell $(x_{j-1/2} + \alpha \Delta x)$ and its location is changing with time. As a consequence, ϵ in the Eq. (7) is a function of time t. For a moving shock with constant speed, $\alpha(t)$ is a periodic function, and the period is equal to the time interval for the shock to cross a numerical cell,

$$T = \frac{\Delta x}{U_s},$$

where U_s is the shock speed. So, the pulsating shock structure from Eq. (7) with unsteady viscosity coefficient generates postshock oscillations. Similar conclusion have been obtained in [6].

The continuing variation of kinetic energy due to averaging in the shock layer exerts a forcing term on the downstream flow motion, which is similar to perturbing one end of a string. The oscillations are generated and propagate along the string. As pointed out by Karni and Canic [7], this behavior is only related to the momentum spike superficially. Physically, even without the mass diffusion term in the continuity equation (7) and with monotonic momentum distribution, the postshock oscillations will still be generated due to the unsteady nature in the momentum and energy equations. This is probably the reason why the momentum spike can be eliminated through a simple transformation $\rho u \rightarrow \rho u - \epsilon \partial_x \rho$, but the postshock oscillations will remain the same [6]. We can validate the above observation in the following example. If applying the projection model to the moving contact discontinuity wave, we can get the same mass diffusion term in the continuity equation and consequently obtain the momentum spike. However, we will not find any numerical oscillations here, because there is no time-dependent nonlinear dissipative mechanism in the momentum and energy equations. Due to the equal velocities $U_1 = U_2$ on both sides of the contact discontinuity, $\Delta E_k = 0$ in Eq. (6) holds.

Based on the projection dynamics, we can explain the relation between the postshock oscillation amplitude and the shock speed. As observed in [2, 10], the very slow and fast
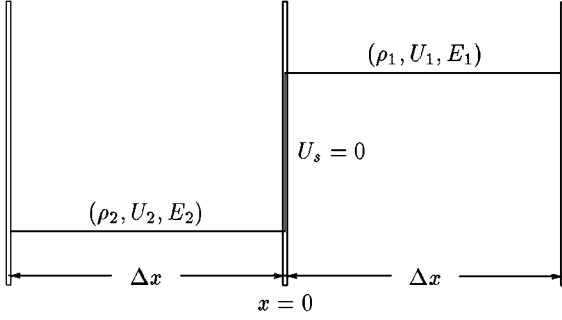
FIG. 2. Stationary shock located at $x = 0$.

moving shocks generate less oscillations. In order to qualitatively evaluate the relation, let us consider the following model. Initially a stationary shock is located at cell interface $x = 0$ with distributions (ρ_2, U_2, E_2) and (ρ_1, U_1, E_1) on the left and right sides, as shown in Fig. 2. The upstream and downstream flow conditions are

$$
\begin{aligned}
\rho_1 &= 1, \\
U_1 &= -1, \quad x \geq 0, \\
P_1 &= \frac{1}{\gamma M^2}.
\end{aligned}
\tag{9}
$$

and

$$
\begin{aligned}
\rho_2 &= \frac{(\gamma + 1)M^2}{2 + (\gamma - 1)M^2} \rho_1, \\
U_2 &= \left(\frac{\gamma - 1}{\gamma + 1} + \frac{2}{(\gamma + 1)M^2} \right) U_1, \quad x \leq 0, \\
P_2 &= \left(\frac{2\gamma}{\gamma + 1} M^2 - \frac{\gamma - 1}{\gamma + 1} \right) P_1,
\end{aligned}
\tag{10}
$$

where M is the upstream Mach number. From the above flow conditions, we can get the sound speeds C_1 and C_2 on both sides,

$$
C_1 = \sqrt{\gamma P_1 / \rho_1}, \quad C_2 = \sqrt{\gamma P_2 / \rho_2}.
$$

For a moving shock, the flow velocities will be changed; i.e., $U_1 \to U_1 + U_s$ and $U_2 \to U_2 + U_s$, where U_s is the shock speed. After each time step Δt, the shock front will be located at $U_s \Delta t$, see Fig. 3. In the numerical cell with shock, the lost kinetic energy due to the averaging is

$$
\Delta E_k = \frac{1}{4} \frac{\rho_1 \Delta t U_s \rho_2 (\Delta x - \Delta t U_s)}{\rho_1 \Delta t U_s + \rho_2 (\Delta x - \Delta t U_s)} (U_1 - U_2)^2 \quad \text{for } U_s > 0.
\tag{11}
$$

Based on the CFL condition (CFL number = 1), the time step is

$$
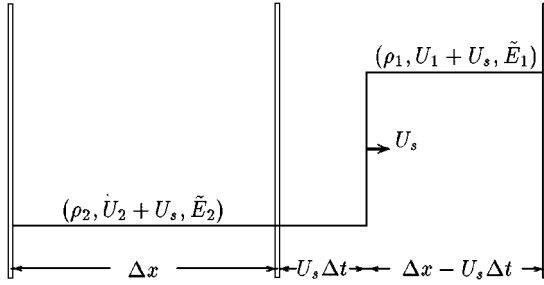\Delta t = \frac{\Delta x}{\text{Max}(|U_1 + U_s| + C_1, |U_2 + U_s| + C_2)},
$$

FIG. 3. Moving shock with speed U_s at time Δt.

and Eq. (11) goes to

$$\Delta E_k = \frac{1}{4} \frac{\rho_1 \rho_2 U_*(1 - U_*)}{\rho_1 U_* + \rho_2(1 - U_*)}(U_1 - U_2)^2 \Delta x \quad \text{for } U_s > 0, \tag{12}$$

where

$$U_* = \frac{|U_s|}{\text{Max}(|U_1 + U_s| + C_1, |U_2 + U_s| + C_2)}.$$

Similarly, for $U_s < 0$ we have

$$\Delta E_k = \frac{1}{4} \frac{\rho_1 \rho_2 (1 - U_*)U_*}{\rho_1(1 - U_*) + \rho_2 U_*}(U_1 - U_2)^2 \Delta x \quad \text{for } U_s < 0. \tag{13}$$

Because the kinetic energy variation in the shock layer perturbs the flow motion, all noises generated in the shock region propagate downstream. The ratio of the energy variation $\Delta E_k \cdot \Delta x$ to the total downstream energy density $\tilde{E}_2$ in each cell is

$$\frac{\Delta E_k}{\tilde{E}_2 \cdot \Delta x} = \frac{\frac{1}{4} \frac{\rho_1 \rho_2 U_*(1 - U_*)}{\rho_1 U_* + \rho_2(1 - U_*)}(U_1 - U_2)^2}{\frac{1}{2}\rho_2(U_2 + U_s)^2 + \frac{1}{\gamma - 1}P_2} \quad \text{for } U_s > 0; \tag{14}$$

similarly,

$$\frac{\Delta E_k}{\tilde{E}_2 \cdot \Delta x} = \frac{\frac{1}{4} \frac{\rho_1 \rho_2 (1 - U_*)U_*}{\rho_1(1 - U_*) + \rho_2 U_*}(U_1 - U_2)^2}{\frac{1}{2}\rho_2(U_2 + U_s)^2 + \frac{1}{\gamma - 1}P_2} \quad \text{for } U_s < 0. \tag{15}$$

The energy fluctuation ratios in (14) and (15) depend mainly on the relative shock speed and velocities. Because of the independence of $\Delta E_k / \tilde{E}_2 \cdot \Delta x$ on the numerical cell size Δx, the postshock oscillations can never be eliminated by refining the mesh. Figure 4 is the plot of relative energy variation $\Delta E_k / \tilde{E}_2 \cdot \Delta x$ versus the relative shock speed $\text{Sign}(U_s)U_*$ for different Mach numbers. The relative energy fluctuation is smaller at both lower and higher shock speeds. From the definition of total energy density $E = \frac{1}{2}\rho U^2 + (1/(\gamma - 1))P$, we can derive the energy variation

$$\Delta E = \rho U \Delta U + \frac{1}{2}U^2 \Delta \rho + \frac{1}{\gamma - 1}\Delta P.$$

Therefore, using $C^2 \sim \gamma \Delta P / \Delta \rho$ and the Riemann invariant $\Delta U \sim \Delta P / \rho C$, we have

$$\Delta E \sim \Delta \rho \left(\frac{|U|C}{\gamma} + \frac{1}{2}U^2 + \frac{C^2}{\gamma(\gamma - 1)} \right),$$
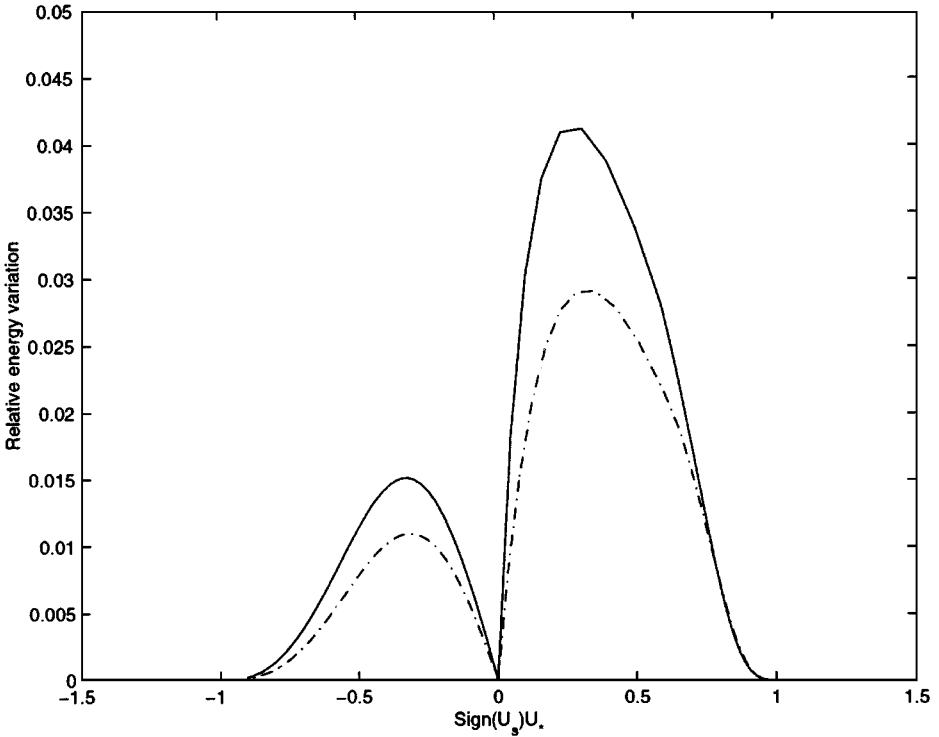
FIG. 4. Relative energy variations $\Delta E_k / \tilde{E}_2 \cdot \Delta x$ versus relative shock speed $\mathrm{Sign}(U_s)U_*$ for different Mach number M; dash-dotted line $M = 3.0$, solid line $M = 20.0$.

from which the density fluctuation in the downstream can be obtained,

$$\frac{\Delta \rho}{\rho_2} = \frac{1}{\rho_2} \left[\left(\frac{\Delta E_k}{\Delta x} \right) \bigg/ \left(\frac{|(U_2 + U_s)|C_2}{\gamma} + \frac{1}{2}(U_2 + U_s)^2 + \frac{C_2^2}{\gamma(\gamma - 1)} \right) \right].$$

Figure 5 is the plot of density fluctuation for different Mach numbers. The numerical observations presented in [2, 10] confirm qualitatively the above theoretical analysis, where there is about 3–5% density variation. In real flow computations, the fast moving shock creates high frequency modes which are decaying much faster than low frequency modes due to the dissipation in both gas evolution and projection stage. As a result, the observational amplitude in the density variation has to be modified by considering the numerical dissipation in the whole downstream region. Also, the shock layer is smeared over several mesh points and the intermediate states in the shock layer are different from the upstream and downstream flow conditions. The final observation should be a statistical averaging over all possible states in the shock layer.

Remarks. The postshock oscillations have been well-explained in the literatures [2, 6, 7, 14]. The current study is based on the projection dynamics rather than specific schemes. In order to understand this problem further, we need to consider the real physical properties in the shock region. Most shock capturing schemes smear the shock layer over a few grid points. The transition region in the shock layer has to be considered as points inside a shock structure. In other words, the intermediate points have intrinsic physical dissipative character, and the flux calculation across each cell interface has to be based on the nonequilibrium
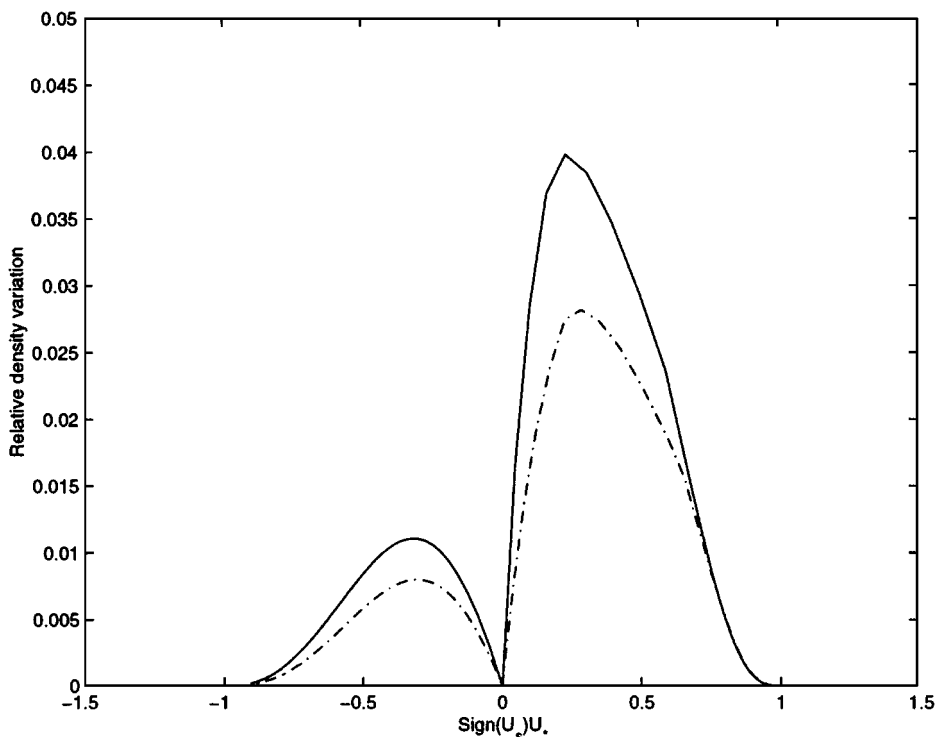
FIG. 5. Relative density variations $\Delta\rho/\rho_2$ versus relative shock speed $\text{Sign}(U_s)U_*$ for different Mach number M; dash-dotted line $M = 3.0$, solid line $M = 20.0$.

Navier–Stokes equations. So, the idea of solving the Euler equations in this region is not physically appropriate [14]. For example, in the first-order BGK scheme, the nonequilibrium Boltzmann equation is solved, which gives sharp and oscillation-free shock transition [19].

To have a consistent dissipative mechanism for the flux function in the numerical shock region is critical for any high resolution schemes; otherwise gigantic amount of viscosity is needed to smear a shock layer in order to get a smooth transition. It is reasonable for Karni and Canic to add viscosity in Roe's Riemann solver to reduce the amplitude in the postshock oscillations [7]. However, without a viscous governing equation for the construction of numerical shock structure, it is very difficult to determine the amount of dissipation needed. Arora and Roe concluded that the oscillation is due to the fact that the intermediate states in the shock regions are not located on the Hugoniot curve [2]. This conclusion is based mainly on the Euler equations. For the viscous governing equations, the states inside the shock layer indeed would not stay on the Hugoniot curve, but they will not generate oscillations if the dissipative term in the flux function can generate a smooth shock transition, such as the BGK scheme [19].

In conclusion, the dynamical effects in the projection stage for the nonlinear system provides the unsteady dissipative mechanism to transfer kinetic energy into thermal energy. This feature is only observed in the nonlinear system. It seems that we have to change the idea that any good numerical techniques for solving the linear wave equation $(U_t + aU_x = 0)$ could be extended by a simple mechanism into equally good numerical techniques for solving system of nonlinear conservation laws $\mathbf{U}_t + \mathbf{F}(\mathbf{U})_x = 0$.
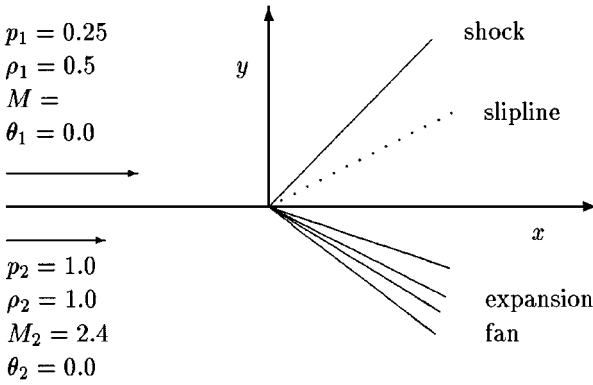
$p_1 = 0.25$
$\rho_1 = 0.5$
$M =$
$\theta_1 = 0.0$

$p_2 = 1.0$
$\rho_2 = 1.0$
$M_2 = 2.4$
$\theta_2 = 0.0$

shock

slipline

expansion
fan

y

x

FIG. 6. 2D Riemann problem.

4. DENSITY FLUCTUATION IN 2D SHEAR WAVE

The idea of projection dynamics presented in Section 2 can be used to explain the density fluctuations in the 2D shear wave. First, let us consider a 2D test case, where the initial flow conditions are shown in Fig. 6 [5]. From these initial conditions, three waves will be formed. They include a shock, a slip line, and an expansion fan.

Using a second-order TVD scheme [15], the density distributions across these waves in the y direction are shown in Fig. 7, where $M = 7$ is used for the initial Mach number for the flow in the upper part. The circles are numerical solutions and the solid lines are exact solutions.

The density fluctuation around slip line in the above figure is a common numerical phenomenon for all shock capturing schemes. In order to understand this, we have to consider the projection dynamics again in the 2D case. As a simple model, we consider a numerical cell which includes the slip line, as shown in Fig. 8. Here the velocities in the direction parallel to the cell interface are not equal, $V_1 \neq V_2$, due to the slip condition and $U_1 = U_2$
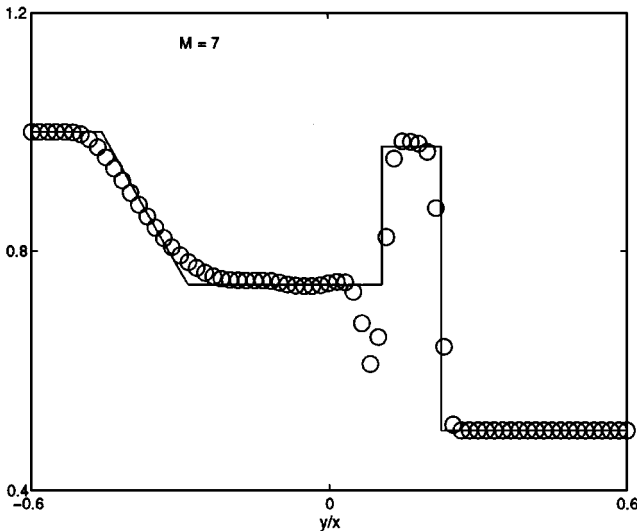
$M = 7$

1.2

0.8

0.4
-0.6   0   0.6
                                       y/x

FIG. 7. Density distribution for the case with Mach number $M = 7$, where the solid line is the exact solution.
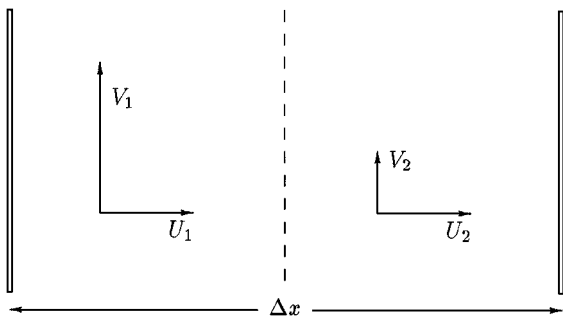
FIG. 8.   Slip line inside a numerical cell.

holds in the normal direction. During the dynamical averaging, the kinetic energy is not conserved. Based on the similar analysis in the 1D case, we can get the kinetic energy loss in the averaging process,

$$\Delta E_k = \frac{1}{4} \frac{\rho_1 \rho_2}{\rho_1 + \rho_2} (V_2 - V_1)^2, \tag{16}$$

where the location of slip line is assumed to be at the center of the numerical cell. From the total energy conservation, the lost kinetic energy has to be transferred into thermal energy and heats the gas around the slip region. The magnitude of heating depends on the relative slip velocities. Due to this heating effect, the temperature and pressure around the slip line will increase. As a consequence, the increased pressure pushes the gas away from each other, and a density sink is formed, as shown in Fig. 7. The artificial heating effects can also be regarded as a result from the friction between different fluids around the slip line. In the 1D case, we cannot observe this phenomenon, because the equal velocity, $U_1 = U_2$, at contact discontinuity prevents the kinetic energy from being transferred into thermal energy. In conclusion, the projection stage introduces a viscous effect and an artificial heating effect in multidimensional flow calculations. The artificial heating effects have also been studied by Noh [12], where the Lagrangian formulation with the explicit form of artificial viscosity automatically creats heating effects next to the boundary.

5. PRESSURE WIGGLES AROUND MATERIAL INTERFACE IN TWO-COMPONENT GAS FLOW

It is observed that for conservative Godunov-type schemes, pressure wiggles at material interface are generated [1]. There exist many explanations for this, such as [8, 9] and references therein. Instead of focusing on the specific flow solver, we will concentrate on the projection dynamics again. Suppose a material interface is located inside a numerical cell and separates the whole cell into two parts with volumes V_1 and V_2, as shown in Fig. 9. The mass, momentum, energy densities, and specific heat ratio in both parts are

$$\left(\rho^{(1)}, \rho^{(1)} U^{(1)}, E^{(1)}, \gamma^{(1)}\right)$$

and

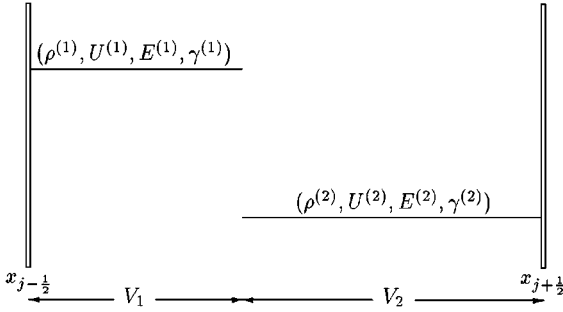$$\left(\rho^{(2)}, \rho^{(2)} U^{(2)}, E^{(2)}, \gamma^{(2)}\right).$$

FIG. 9. Multicomponent subcell mixing at material interface.

The material interface is a contact discontinuity with equal velocities, $U^{(1)} = U^{(2)}$, and equal pressures, $P^{(1)} = P^{(2)}$. In order to simplify the derivation, we assume $U^{(1)} = U^{(2)} = 0$ here. This assumption will not change the applicability of the following analysis to the general cases around a moving material interface.

The projection stage mixes different components and the mixing is based on the total mass, momentum and energy conservations. Since the momentum equation can be ignored here due to the equal velocities in the two components, the mass and energy conservations will be used. They are

$$\rho^{(1)} V_1 + \rho^{(2)} V_2 = \rho(V_1 + V_2) \tag{17}$$

and

$$E^{(1)} V_1 + E^{(2)} V_2 = E(V_1 + V_2). \tag{18}$$

For a perfect gas, energy conservation reduces to

$$\frac{kT^{(1)}}{\gamma^{(1)} - 1} \frac{\rho^{(1)} V_1}{m_1} + \frac{kT^{(2)}}{\gamma^{(2)} - 1} \frac{\rho^{(2)} V_2}{m_2} = T \left(\frac{k}{\gamma^{(1)} - 1} \frac{\rho^{(1)} V_1}{m_1} + \frac{k}{\gamma^{(2)} - 1} \frac{\rho^{(2)} V_2}{m_2} \right), \tag{19}$$

where k is Boltzmann constant, m_1 and m_2 are the molecular masses for gas 1 and gas 2, $T^{(1)}$, $T^{(2)}$, and T are the temperatures of the initial two components and the final equilibrium state. From Eq. (19), the common temperature after mixing (with the assumption $m_1 = m_2$) can be obtained,

$$T = \frac{(\gamma^{(2)} - 1)T^{(1)} \rho^{(1)} V_1 + (\gamma^{(1)} - 1)T^{(2)} \rho^{(2)} V_2}{(\gamma^{(2)} - 1)\rho^{(1)} V_1 + (\gamma^{(1)} - 1)\rho^{(2)} V_2}. \tag{20}$$

The final pressure $\tilde{P}$ in the whole cell $(V_1 + V_2)$ becomes

$$\begin{aligned} \tilde{P} &= \tilde{P}^{(1)} + \tilde{P}^{(2)} \\ &= \frac{V_1}{V_1 + V_2} \frac{T}{T^{(1)}} P^{(1)} + \frac{V_2}{V_1 + V_2} \frac{T}{T^{(2)}} P^{(2)} \\ &= \frac{TP}{V_1 + V_2} \left(\frac{V_1}{T^{(1)}} + \frac{V_2}{T^{(2)}} \right), \end{aligned} \tag{21}$$

where $\tilde{P}^{(1)}$ and $\tilde{P}^{(2)}$ are the partial pressure contributions from components 1 and 2 gases separately after mixing, and $P = P^{(1)} = P^{(2)}$ are the initial individual gas pressures before mixing. Substituting Eq. (20) into Eq. (21), we obtain

$$\tilde{P} = P \frac{V_1 T^{(2)} + V_2 T^{(1)}}{T^{(1)} T^{(2)} (V_1 + V_2)} \frac{(\gamma^{(2)} - 1) T^{(1)} \rho^{(1)} V_1 + (\gamma^{(1)} - 1) T^{(2)} \rho^{(2)} V_2}{(\gamma^{(2)} - 1) \rho^{(1)} V_1 + (\gamma^{(1)} - 1) \rho^{(2)} V_2}. \tag{22}$$

Obviously, $\tilde{P} \neq P$ in general cases, which means that the final pressure after mixing is different from the initial pressure at the material interface. Once the pressure variation is formed near the material interface, it subsequently generates waves and contaminates the flow field . For a single component gas, ($\gamma^{(1)} = \gamma^{(2)}$), Eq. (22) gives $\tilde{P} = P$ automatically, and the equal pressure is kept. An alternative explanation for the above phenomena can be the following. For an ideal gas, each degree of freedom in a molecule has an equal amount of energy which is proportional to temperature T. The total internal energy for each molecule is $e^{(1)} = kT^{(1)}/(\gamma^{(1)} - 1)$ for component 1 gas, and $e^{(2)} = kT^{(2)}/(\gamma^{(2)} - 1)$ for component 2 gas. Suppose that by collisions these two molecules exchange their energies and equalize their temperature to a common one T. From energy conservation, we have

$$\frac{k\Delta T^{(1)}}{\gamma^{(1)} - 1} + \frac{k\Delta T^{(2)}}{\gamma^{(2)} - 1} = \Delta E^{(1)} + \Delta E^{(2)} = 0. \tag{23}$$

However, the pressure change due to temperature variation is

$$\Delta P \sim k\Delta T^{(1)} + k\Delta T^{(2)} = k\frac{\gamma^{(1)} - \gamma^{(2)}}{\gamma^{(1)} - 1} \Delta T^{(1)}$$
$$= \left(\gamma^{(1)} - \gamma^{(2)}\right) \Delta E^{(1)} = \left(\gamma^{(2)} - \gamma^{(1)}\right) \Delta E^{(2)}, \tag{24}$$

which cannot be zero if $\gamma^{(1)} = \gamma^{(2)}$ is not satisfied.

6. CONCLUSION

In this paper, we have analyzed the projection dynamics in Godunov-type schemes. The projection process is a purely numerical aspect due to the limited cell size and time step. However, it provides dynamical influence on the flow motion. Based on this, a few anomalous phenomena are explained, which include postshock oscillations, density fluctuation at a slip line, and pressure wiggles at a material interface. It is concluded that the schemes based on the exact Riemann solver will not yield robust and accurate schemes, where the projection errors cannot be eliminated by considering the inviscid Euler solution in the gas evolution stage. Unless the fluxes in the Riemann solver are augmented by consistent physical dissipation, any Godunov-type schemes will be flawed. Other spurious solutions, such as carbuncle phenomena and odd–even decoupling, can be explained by the combination of the projection and gas evolution dynamics. It is realized that the carbuncle phenomena and odd–even decoupling is intrinsically rooted in the Godunov method once the inviscid Euler equations are solved in the gas evolution stage [18]. So, a positive suggestion from this paper is that we have to find and solve a viscous governing equation directly in the gas evolution stage in order to avoid spurious solutions, rather than keep on fixing the existing flux function. The modification of the exact Riemann solver to get more robust numerical

schemes is actually a process to solve some other equations, although we do not explicitly mention it. The gas-kinetic BGK model probably provides such an equation [17].

APPENDIX A: THE DERIVATION OF THE GOVERNING EQUATIONS

Figure 1 outlines the projection process in an isolated cell from the initial flow distribution to the final constant state. This process is finished in a whole time step Δt. In the following, we are going to derive the approximate governing equations in this process. At end, the convective fluxes from the gas evolution stage will be added.

(1) *Continuity equation.* In subcell $x\epsilon[x_{j-1/2}, x_{j-1/2} + \alpha\Delta x]$, density is changed from the initial ρ_1 to the final $\bar\rho = \alpha\rho_1 + (1-\alpha)\rho_2$ through the mass fluxes at $x = x_{j-1/2}+\alpha\Delta x$. If we assume that the mass flux is equal to $\eta_1\rho_x$, we have

$$\frac{\bar\rho - \rho_1}{\Delta t} = \frac{\eta_1\rho_x}{\alpha\Delta x} = \frac{\eta_1(\rho_2 - \rho_1)}{\alpha\Delta x\frac{1}{2}\Delta x}, \tag{25}$$

from which the mass diffusion coefficient η_1 can be obtained $\eta_1 = \frac{1}{2}\alpha(1 - \alpha)((\Delta x)^2/\Delta t)$.

(2) *Momentum equation.* In subcell $x\epsilon[x_{j-1/2}, x_{j-1/2} + \alpha\Delta x]$ again, the initial momentum $\rho_1 U_1$ is changed to $\bar\rho\bar U$ in a time step Δt. Denoting the viscous flux as $\eta_2 U_x$, we have

$$\frac{\bar\rho\bar U - \rho_1 U_1}{\Delta t} = \frac{\alpha\rho_1 U_1 + (1-\alpha)\rho_2 U_2 - \rho_1 U_1}{\Delta t} = \frac{\eta_2 U_x}{\alpha\Delta x} = \frac{\eta_2(U_2 - U_1)}{\alpha\Delta x\frac{1}{2}\Delta x}. \tag{26}$$

With the assumption

$$\rho_2 U_2 - \rho_1 U_1 \sim \rho(U_2 - U_1),$$

we have

$$\eta_2 = \frac{1}{2}\alpha(1 - \alpha)\frac{(\Delta x)^2}{\Delta t}\rho.$$

(3) *Energy equation.* The dissipative effect in the energy equation is to transfer the kinetic energy into the thermal energy. In the whole numerical cell, we can write down the energy dissipation process as

$$\frac{\partial E_k}{\partial t} = (\eta_3 U U_x)_x.$$

From the above equation and Eq. (6), we have

$$\frac{\Delta E_k}{\Delta t} = \frac{\frac{1}{4}\frac{\alpha\rho_1(1-\alpha)\rho_2}{\alpha\rho_1+(1-\alpha)\rho_2}(U_2 - U_1)^2}{\Delta t} = \eta_3\frac{(U_2 - U_1)U_x}{\frac{1}{2}\Delta x} = \eta_3\frac{(U_2 - U_1)^2}{\frac{1}{2}\Delta x\frac{1}{2}\Delta x}.$$

So, with the assumption

$$\frac{\rho_1\rho_2}{\alpha\rho_1 + (1-\alpha)\rho_2} \sim \rho,$$

we obtain

$$\eta_3 = \frac{1}{16}\alpha(1-\alpha)\frac{(\Delta x)^2}{\Delta t}\rho.$$

While the projection stage provides the mechanism to smear the subcell structure, the gas evolution stage accounts the external influence through the numerical fluxes across the cell interface. If the Euler equations are exactly solved in the gas evolution stage, the mass, momentum, and energy transports through a cell interface are $(\rho U, \rho U^2 + P, EU + PU)$. Combining the Euler fluxes with the diffusion and dissipative terms in the projection stage, we can get the "Navier–Stokes" equations for the updating of flow variables in the Godunov-type schemes,

$$\rho_t + (\rho U)_x = \epsilon \rho_{xx},$$
$$(\rho U)_t + (\rho U^2 + P)_x = \epsilon(\rho U_x)_x,$$
$$E_t + (EU + PU)_x = \frac{1}{8}\epsilon(\rho U U_x)_x,$$

where

$$\epsilon = \frac{1}{2}\alpha(1-\alpha)\frac{(\Delta x)^2}{\Delta t}.$$

ACKNOWLEDGMENTS

REFERENCES

1. R. Abgrall, How to prevent pressure oscillations in multicomponent flow calculations: A quasi conservative approach, *J. Comput. Phys.* **125**, 150 (1996).

2. M. Arora and P. Roe, On post-shock oscillations due to shock capturing schemes in unsteady flows, *J. Comput. Phys.*, to appear.

3. P. Colella and P. Woodward, The piecewise parabolic method (PPM) for gas dynamical calculations, *J. Comput. Phys.* **54**, 174 (1984).

4. D. Gilbarg and D. Paolucci, The structure of shock waves in the continuum theory of fluids, *J. Rational Mech. Anal.* **2**, 617 (1953).

5. W. H. Hui, *Accurate Computation of Discontinuous Flow—The Role of Coordinates*, 2nd Asia CFD Conference, Tokyo, 1996.

6. S. Jin and J. Liu, The effects of numerical viscosity I: Slowly moving shocks, *J. Comput. Phys.* **126**, 373 (1996).

7. S. Karni and S. Canic, Computations of slowly moving shocks, *J. Comput. Phys.* **136**, 132 (1997).

8. S. Karni, Multicomponent flow calculations by a consistent primitive algorithm, *J. Comput. Phys.* **112**, 31 (1994).

9. B. Larrouturou, How to preserve the mass fraction positive when computing compressible multi-component flow, *J. Comput. Phys.* **95**, 59 (1991).

10. H. C. Lin, Dissipation additions to flux-difference splitting, *J. Comput. Phys.* **117**, 20 (1995).

11. M. S. Liou, Probing numerical fluxes: Mass flux, positivity, and entropy-satisfying property, AIAA 97-2035 (1997).

12. W. F. Noh, Errors for calculations of strong shocks using an artificial viscosity and an artificial heat flux, *J. Comput. Phys.* **72**, 78 (1987).

13. J. Quirk, A contribution to the great Riemann solver debate, *Int. J. for Num. Methods in Fluids* **18**, 555 (1994).

14. T. W. Roberts, The Behavior of flux difference splitting near slowly moving shock waves, *J. Comput. Phys.* **90**, 141 (1990).

15. P. R. Sweby, High resolution schemes using flux limiters for hyperbolic conservation laws, *SIAM J. Num. Anal.* **21**, 995 (1984).

16. P. Woodward and P. Colella, The numerical simulation of two-dimensional fluid flow with strong shocks, *J. Comput. Phys.* **54**, 115 (1984).

17. K. Xu, L. Martinelli, and A. Jameson, Gas-kinetic finite volume methods, flux-vector splitting and artificial diffusion, *J. Comput. Phys.* **120**, 48 (1995).

18. K. Xu, "*Gas-Kinetic Schemes for Unsteady Compressible Flow Simulations*," 29th Computational Fluid Dynamics, Lecture Series 1998–03, von Karman Institute (1998).

19. K. Xu and J. Hu, Projection dynamics in Godunov-type schemes: To the physical understanding of postshock oscillations, `http://www.math.ntnu.no/conservation/`, Preprints on Conservation Laws 1997-001.

20. Ya. B. Zel'dovich and Yu. P. Raizer, *Physics of Shock Waves and High-Temperature Hydrodynamic Phenomena* (Academic Press, New York, 1966).